Materials Advances

ROYAL SOCIETY OF CHEMISTRY

PAPER

View Article Online
View Journal | View Issue

Cite this: *Mater. Adv.*, 2026, 7, 1127

A comparative study of medium-entropy oxide and metal oxide nanoparticles on graphene oxide for benzyl alcohol oxidation under solvent-free conditions

Seyedsaeed Mehrabi-Kalajahi, *[ab] Seyed Amir Hossein Vasigh,[a] Behrouz Shaabani, *[a] Hassan Yousefi Bavili,[c] Ahmad Ostovari Moghaddam,[d] Ameen Al-Muntaser[b] and Mikhail A. Varfolomeev[b]

A series of monometallic catalysts, such as Fe_3O_4, CoO, NiO, and CuO, along with their entropy-stabilized nanoparticles [$(Fe,Co,Ni,Cu)_3O_4$ medium-entropy oxide (MEO)], were synthesized and subsequently utilized for the solvent-free and selective aerobic oxidation of benzyl alcohol when supported on graphene oxide (GO). The resulting nanocomposites underwent characterization through various techniques including X-ray diffraction (XRD), scanning electron microscopy (SEM), atomic force microscopy (AFM), transmission electron microscopy (TEM), Brunauer–Emmett–Teller (BET) analysis, thermogravimetric analysis (TGA), Raman spectroscopy, and X-ray photoelectron spectroscopy (XPS), which collectively confirmed the successful formation of monometallic and spinel $(Fe,Co,Ni,Cu)_3O_4$ MEO nanoparticles integrated into GO. Among the utilized catalysts, the $(Fe,Co,Ni,Cu)_3O_4$ MEO–GO nanoparticles exhibit remarkable catalytic efficiency. A conversion rate of up to 17.2% and 28.8%, along with selectivity rates of 71.4% and 65.7% for benzaldehyde, can be attained in just 5 h at air pressures of 1 and 10 atm, respectively. A comprehensive analytical investigation indicates that the remarkable performance of $(Fe,Co,Ni,Cu)_3O_4$ MEO–GO nanocomposites can be ascribed to the synergistic interaction between the active sites of GO and the plentiful oxygen vacancies present in the $(Fe,Co,Ni,Cu)_3O_4$ MEO nanoparticles. The exceptional catalytic behavior of $(Fe,Co,Ni,Cu)_3O_4$ MEO–GO nanocomposites is attributed, according to detailed analyses, to the synergy between GO active sites and the numerous oxygen vacancies within the MEO nanoparticles. In summary, the extensive experimental findings indicate the promising use of $(Fe,Co,Ni,Cu)_3O_4$ MEO–GO nanocomposites within the chemical sector for the targeted oxidation of alcohols into high-value products.

Received 20th September 2025,
Accepted 30th November 2025

DOI: 10.1039/d5ma01075f

rsc.li/materials-advances

1. Introduction

The selective oxidation of alcohols to aldehydes represents a critical transformation in fine chemical synthesis, particularly for converting benzyl alcohol to benzaldehyde—a vital intermediate in pharmaceutical, agrochemical, and fragrance industries. This challenging reaction requires precise cleavage of O–H bonds followed by C–H activation while preventing overoxidation to carboxylic acids. The process gains industrial significance as benzaldehyde serves as a key building block for manufacturing drugs, agrochemicals, perfumes, and dyes.[1–3] The conventional method typically involves the use of harmful organic solvents like acetonitrile and toluene, along with dangerous oxidizing agents such as dichromate, peroxide, and permanganate, leading to significant environmental concerns.[4–6] Consequently, the catalytic oxidation of benzyl alcohol using molecular oxygen as an environmentally friendly and cost-effective oxidant is regarded as a sustainable synthesis pathway with significant promise for the production of benzaldehyde. Noble metals such as gold (Au) and palladium (Pd) exhibit outstanding catalytic activity for the oxidation of benzyl alcohol under relatively mild conditions. However, their scarcity and high cost significantly limit their feasibility for large-scale utilization. As an example, the Au_1Pd_1/CNT bimetallic nanocomposite catalyst has been reported to oxidize benzyl alcohol to benzaldehyde under alkali-free conditions with a selectivity of 91.8%.[7–9] Metal oxides are absolutely crucial as heterogeneous catalysts for industrial oxidation reactions, thriving in petrochemical processes and the synthesis of

[a] *Department of Inorganic Chemistry, University of Tabriz, Tabriz, Iran. E-mail: shaabani.b@gmail.com, shaabani@tabrizu.ac.ir*
[b] *Department of Petroleum Engineering, Kazan Federal University, Kazan, 420008, Russia. E-mail: ss.mehrabikalajahi@gmail.com, smehrabi.kaladzhahi@kpfu.ru*
[c] *Department of Chemical & Biomolecular Engineering, University of Houston, Houston, TX, 77204, USA*
[d] *HSE University, Moscow, 101000, Russia*

specialty chemicals. Moreover, they are indispensable in the treatment of pollutants, especially for adjusting selectivity to minimize by-products.[10–12] The development of reliable heterogeneous catalysts for solvent-free aerobic alcohol oxidation under mild conditions represents a critical need in sustainable chemistry, particularly for selective transformations such as the conversion of benzyl alcohol to benzaldehyde. Transition metal oxides offer an ideal platform for these reactions, combining earth abundance with tunable redox properties that facilitate selective C–H bond activation while suppressing over-oxidation. Their exceptional adaptability in oxygen-mediated transformations—from primary alcohol oxidation to selective amine functionalization—stems from modifiable surface oxygen vacancies and adaptable electronic structures.[13,14] Shi *et al.* suggested that manganese dioxides exhibiting various crystal structures, specifically α-, β-, γ-, and δ-MnO_2 catalysts, serve as effective metal oxides for the selective oxidation of benzyl alcohol to benzaldehyde. Their findings indicated that β-MnO_2, characterized by a high surface area, achieved the greatest conversion of benzyl alcohol relative to the other structures, which can be attributed to its elevated number of oxygen vacancies.[15] In a separate study, Hu *et al.* prepared mesoporous nickel oxide, cobalt oxide, and mixed nickel–cobalt oxides with various Ni/Co ratios for the catalytic oxidation of benzyl alcohol in the presence of DMF as the solvent. The mixed oxides showed superior activity compared to the monometallic counterparts, with Ni_1Co_3 (Ni/Co = 1/3) performing the best due to its high density of oxygen vacancies. Their results indicated that Ni_1Co_3 achieved over 90% conversion, though only when the reaction was conducted at 120 °C for 8 hours, reflecting its need for a relatively high temperature and extended reaction time to reach optimal efficiency.[16] Furthermore, latest studies indicate that combining transition-metal oxides with graphene-based supports—forming metal oxide@GO or metal oxide@rGO hybrids—can significantly enhance catalytic performance.[17,18] GO provides abundant functional groups for uniform metal oxide dispersion, while rGO offers superior electrical conductivity, enabling faster electron transfer and stabilizing oxygen vacancies.[19] These synergistic effects improve reactant adsorption, redox activity, and structural stability, allowing such hybrids to achieve high conversion under milder conditions compared to bare metal oxides.

Recent studies have increasingly focused on high-entropy oxides (HEOs) and medium-entropy oxides (MEOs) due to their significant potential as heterogeneous catalysts, offering superior catalytic performance and enhanced product selectivity compared to conventional single-component metal catalysts.[20–27] A medium-entropy oxide (MEO), defined as a multicomponent oxide with three or four near-equimolar cations and a configurational entropy between 1.0R and 1.5R (where R is the gas constant), exhibits intermediate structural and property tunability between low- and high-entropy oxides. The lattice potential energy variation from differing atomic environments increases atomic migration barriers, enhancing catalytic stability,[28] while the strategic integration of multiple components enables advanced design and optimization of novel catalytic systems, positioning HEOs and MEOs as highly promising candidates in heterogeneous catalysis.[29] In 2022, Fereja and colleagues developed a high entropy oxide (HEO) nanostructure designated as $(FeNiCoCrCu)_3O_4$, characterized by a significant presence of oxygen vacancies, an extensive surface area, and numerous active sites conducive to urea oxidation and oxygen evolution reactions.[30] This innovative synthesis exhibited remarkable performance and stability, underscoring its potential applications in relevant chemical processes. In 2020, Feng and his research team developed a high entropy oxide characterized by the formula $Co_{0.2}Ni_{0.2}Cu_{0.2}Mg_{0.2}Zn_{0.2}O$.[31] This material exhibits a porous lamellar architecture enriched with oxygen vacancies, which collectively contribute to its outstanding catalytic efficiency in the oxidation of benzyl alcohol to value-added products. The major oxidation products were identified as benzaldehyde and benzoic acid, confirming its superior catalytic performance compared with related systems. Notably, the holey-lamellar HEO catalyst shows remarkable activity under solvent-free aerobic conditions, achieving over 90% conversion within 2 hours, with a benzaldehyde selectivity of approximately 29%. Our research has shown that a medium-entropy oxide (MEO) and high entropy oxide (HEO) attached to reduced graphene oxide (rGO) exhibit superior selectivity for the solvent-free aerobic oxidation of toluene and benzyl alcohol within a brief duration, surpassing the performance of catalysts documented in prior studies.[23,26]

In this research, we present a novel and sustainable method for the selective oxidation of benzyl alcohol to benzaldehyde, employing a MEO nanostructure that is supported on graphene oxide (GO) in a solvent-free setting while varying the pressure conditions. Additionally, we conducted a comparative analysis of the MEO and MEO–GO catalysts alongside their respective monoxide and composite forms to evaluate their catalytic performance. The MEO–GO catalyst exhibited conversion rates of 17.2% and 28.8%, achieving remarkable selectivities of 56.3% and 47.1% for benzaldehyde under atmospheric and 10 atm O_2 pressure conditions.

2. Experimental

2.1. Chemicals and experimental methods

The study utilized a variety of materials, including iron(III) chloride hexahydrate ($FeCl_3{\cdot}6H_2O$), iron(II) chloride tetrahydrate ($FeCl_2{\cdot}4H_2O$), cobalt(II) chloride hexahydrate ($CoCl_2{\cdot}6H_2O$), nickel(II) carbonate hydrate CH_2NiO_4, and copper(II) chloride ($CuCl_2{\cdot}2H_2O$). Additionally, 1-octadecene ($C_{18}H_{36}$), sodium hydroxide (NaOH), graphite, sodium nitrate ($NaNO_3$), and potassium permanganate ($KMnO_4$) were sourced from Merck Company in Germany. Deionized water (DIW) was obtained from Ghazi Company based in Tabriz, Iran. Furthermore, solvents such as benzyl alcohol ($C_6H_5CH_2OH$) and hexane (C_6H_{14}), along with sulfuric acid (H_2SO_4), oleic acid ($C_{18}H_{34}O_2$), oxalic acid ($C_2H_2O_4$), hydrochloric acid (HCl), and hydrogen peroxide (H_2O_2), were acquired from Sigma Aldrich.

2.1.1. Synthesis of metal oxide (MO) nanoparticles. Initially, ferric chloride ($FeCl_3 \cdot 6H_2O$) and ferrous chloride ($FeCl_2 \cdot 4H_2O$) were individually dissolved in DIW, maintaining a molar ratio of 2 : 1. Subsequently, the two solutions of Fe(III) and Fe(II) were combined in a three-necked flask and subjected to stirring under an inert nitrogen atmosphere for a duration of 3 h at a temperature of 60 °C. During this stirring process, a 3.5 M solution of NH_4OH was introduced as a precipitating agent. Finally, the resulting mixture was separated and the obtained Fe_3O_4 allowed to dry at room temperature for 12 h.[32] To produce cobalt monoxide nanoparticles, a combination of 2.60 g of cobalt oleate complex, 30 ml of 1-octadecene, and 1.5 ml of oleic acid was placed in a flask and stirred for 2 h at room temperature within a neutral nitrogen environment. The resulting mixture was then gradually heated to a designated temperature, where it was refluxed and aged for 1 h under nitrogen while being continuously stirred mechanically. Following this process, the mixture was allowed to cool to 20 °C, after which it was transferred to centrifuge tubes and then centrifuged at 5000 rpm for 30 min in the presence of a 15 ml mixed solvent of ethanol and hexane in a 1 : 3 volume ratio.[33] In order to synthesize NiO nanoparticles, nickel carbonate hydrate and oxalic acid were thoroughly blended in a 1 : 1 molar ratio through grinding with a mortar and pestle. Subsequently, a suitable quantity of water was added to create a rheological body. This mixture underwent a reaction at a temperature of 100 °C for a duration of 12 h, after which it was washed with both water and ethanol. Finally, the product was subjected to treatment in a furnace at 500 °C.[34] Copper oxide (CuO) nanoparticles were synthesized using copper chloride dihydrate and sodium hydroxide pellets as precursors in an aqueous medium. Initially, 2 g of $CuCl_2 \cdot 2H_2O$ were dissolved in 100 ml of ethanol while stirring continuously at room temperature. Following this, 40 ml of 1 M sodium hydroxide solution in ethanol was added gradually. The mixture was stirred persistently at room temperature to promote the necessary chemical reactions. During this process, the solution's color changed from green to black, indicating the formation of a copper hydroxide precipitate. To ensure that the precipitation reaction was complete, stirring was continued for an additional hour. The resulting sample was then subjected to centrifugation and thoroughly washed with DIW to remove any unreacted materials, after which the collected sediments were calcined at a temperature of 550 °C.[35]

2.1.2. Synthesis of medium-entropy oxide (MEO) nanoparticles. The synthesis of medium-entropy oxide (MEO) nanoparticles typically employs the co-precipitation technique, which begins with the formation of a uniform mixture of metal ions in a solution.[36,37] This mixture is subsequently subjected to high-temperature calcination to yield the desired oxide materials. In the case of synthesizing $(Fe,Co,Ni,Cu)_3O_4$ MEO, an initial step involves dissolving 0.01 mol of Fe(II), Co(II), Ni(II), and Cu(II) chloride salts in 30 ml of deionized water, followed by stirring the solution for 20 min using a mechanical stirrer. Subsequently, a 1 M solution of NH_4OH is introduced into the mixture to adjust the pH to approximately 8.5. After an additional 4 h of stirring, the solution is heated to 160 °C for 12 h in a stainless steel autoclave. The resultant material is subsequently subjected to a calcination procedure at a temperature of 800 °C for a duration of 4 h.

2.1.3. Synthesis of graphene oxide (GO) nanosheets. In this study, we employed Hummers method to synthesize graphene oxide from graphite powder.[38,39] Initially, 1 g of graphite powder was combined with 28 ml of concentrated sulfuric acid and placed in an ice bath to maintain a low temperature. After a stirring period of 20 min, 0.5 g of sodium nitrate was introduced into the mixture, and stirring was continued for an additional 2 h. Subsequently, 3 g of potassium permanganate were gradually incorporated into the mixture over a span of 45 min, followed by another 30 min of stirring. The reaction temperature was then raised to 40 °C by removing the ice bath and placing the flask in an oil bath, after which the mixture was diluted with 40 ml of DIW. The temperature of this diluted solution was further increased to above 90 °C, at which point 150 ml of DIW and 5 ml of hydrogen peroxide were added. The final step involved centrifuging the mixture, followed by washing the resulting precipitate with the mixed hydrochloric acid solution and DIW for a duration of 24 h.

2.1.4. Synthesis of MO–GO and MEO–GO composites. The treatment process involved the utilization of metal oxidation composites, specifically Fe_3O_4, CoO, NiO, and CuO, in conjunction with graphene oxide (MO–GO) and a medium-entropy oxide composite, $(Fe,Co,Ni,Cu)_3O_4$ MEO, which was combined with graphene oxide nanosheets (MEO–GO). A weight ratio of 1 : 3 was established, allocating one part to the metal oxide nanoparticles and medium entropy oxides, while three parts were designated for the graphene oxide nanosheets. This mixture was then dispersed in 60 ml of DIW and subjected to mechanical stirring for 1 h. Subsequently, the resulting mixture was transferred to an autoclave, where 200 ml was added and subjected to autoclaving overnight at a temperature of 140 °C. The final product underwent multiple washes with acetone and was subsequently dried at room temperature.

2.2. Apparatus

The X-ray diffraction (XRD) patterns of the synthesized samples were obtained using a Tongda X-ray diffractometer (TD-3700 Model, China), which employed Cu-Kα radiation (λ = 0.154 nm, 40 kV, 40 mA). Raman scattering provides insights into molecular bonding, resulting in a unique Raman spectrum corresponding to each specific molecular configuration. The morphological characteristics and elemental composition of the samples were examined through field emission scanning electron microscopy (FESEM) using a TESCAN MIRA3 FEG-SEM model, operating at an accelerating voltage of 15 kV, with samples affixed to metal stubs *via* double-sided carbon adhesive tape. Further morphological studies have also explored the use of the atomic force microscope (AFM) system from ARA Research Company (Iran) for nanometer imaging. This instrument offers high resolution and quality imaging capabilities and is designed as a desktop device suitable for a range of applications. All operational modes can be utilized by

assembling the appropriate kit for this device. Additionally, transmission electron microscopy (TEM) analyses were conducted with a Hitachi HT7700 Exalens at 120 kV. X-ray photoelectron spectroscopy (XPS) served as a pivotal technique for the characterization of catalysts utilized in the oxidation reaction process, enabling the assessment of their chemical composition and oxidation states. XPS analyses were performed within an ultra-high vacuum (UHV) chamber, maintaining a base pressure of approximately 5×10^{-10} mbar. The measurements employed an Mg K_α X-ray source operating at 12.5 kV and 250 W, in conjunction with a PHOIBOS 150 hemispherical energy analyzer, all sourced from SPECS GmbH. The ^{1}H NMR (300 MHz, DMSO-d_6) spectra were recorded on a Bruker Avance III 300 MHz spectrometer to characterize the organic compounds formed during the oxidation of benzyl alcohol, using TMS as the internal reference. Details of the separation procedure for benzaldehyde, the major product, are provided in the SI. Electron paramagnetic resonance (EPR) measurements were carried out on a Bruker E500 instrument under X-band conditions (9.41 GHz, 2.0 mW) with a swept magnetic field at room temperature. An Agilent 7890B gas chromatograph, featuring an Agilent J&W GC column that is 30 m long, 0.530 mm in diameter, and has a film thickness of 1.50 mm, was employed to assess the consumption of benzyl alcohol and the formation of oxidized compounds across a temperature spectrum of 60 to 320 °C.

2.3. Catalytic performance

The experiments were carefully designed and carried out to facilitate the selective oxidation of benzyl alcohol under solvent-free conditions. Initially, 5 mL of benzyl alcohol was placed in a 250 mL reaction flask, which was then exposed to atmospheric air under controlled temperature conditions. For the oxidation process, a compressed air cylinder was employed as the oxygen source. The air flow into the reaction flask was precisely monitored and regulated using a pressure gauge to ensure consistent and controlled reaction conditions. The oxidation of benzyl alcohol was subsequently conducted under increased air pressure within a 400 ml autoclave, which was fitted with a mechanical stirrer to ensure proper mixing. Following this initial phase, catalysts at specified concentrations were introduced, along with an additional 5 ml of benzyl alcohol, into the autoclave, where both air pressure and temperature were carefully regulated to maintain consistent stirring throughout the reaction. The assessment of the stability and reusability of the synthesized catalysts was conducted.

3. Results & discussion

3.1. Characterization of the catalysts

Fig. 1a and Fig. S1 display the X-ray diffraction (XRD) patterns of graphene oxide (GO) and its composites with Fe_3O_4, CoO, NiO, CuO, as well as the medium-entropy oxide $(Fe,Co,Ni,Cu)_3O_4$, along with their indexed peaks and corresponding JCPDS reference numbers. The XRD spectra for the combinations of Fe_3O_4–GO, CoO–GO, NiO–GO, and CuO–GO exhibit distinct peaks that are indicative of the respective materials, with specific indices marking their positions, consistent with previously established research on nanoparticles.[40–42] Notably, the XRD analysis of the $(Fe,Co,Ni,Cu)_3O_4$ MEO–GO reveals an entropy-stabilized oxide phase characterized by an inverse spinel structure, devoid of any additional phases, particularly oxides, in the powder XRD pattern.[43] The conventional inverse spinel structure, as seen in Fe_3O_4, is characterized by a distorted face-centered cubic (fcc) lattice of oxygen, where cations occupy one-eighth of the tetrahedral sites and half of the

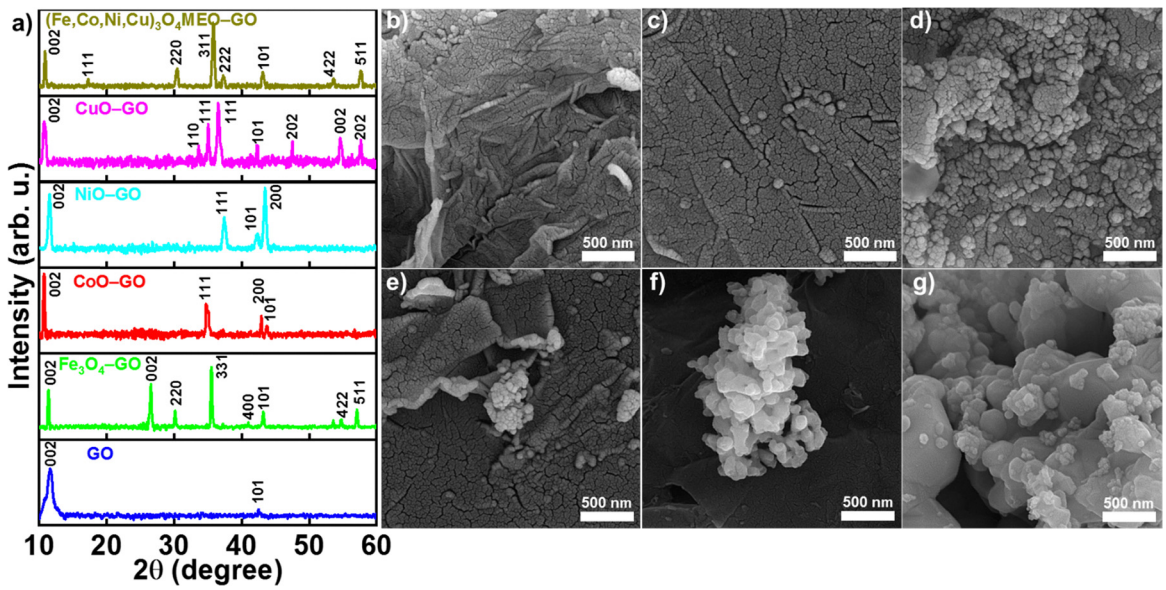

Fig. 1 (a) XRD patterns of GO, Fe_3O_4–GO, CoO–GO, NiO–GO, CuO–GO, and $(Fe,Co,Ni,Cu)_3O_4$ MEO–GO, and the SEM micrographs of (b) GO, (c) Fe_3O_4–GO, (d) CoO–GO, (e) NiO–GO, (f) CuO–GO, and (g) $(Fe,Co,Ni,Cu)_3O_4$ MEO–GO samples.

octahedral sites. It is expected that this structure will undergo slight distortion in the $(Fe,Co,Ni,Cu)_3O_4$ MEO. Additionally, within the lattice of the $(Fe,Co,Ni,Cu)_3O_4$ MEO, four cations are required to occupy the interstitial sites of the fcc lattice, which necessitates the occupation of an extra interstitial site compared to the typical inverse spinel structure. Fig. 1b–g presents scanning electron microscopy (SEM) images of GO, Fe_3O_4–GO, CoO–GO, NiO–GO, CuO–GO, and $(Fe,Co,Ni,Cu)_3O_4$ MEO–GO. The GO displayed a characteristic plate-like morphology with a somewhat elevated level of agglomeration. Conversely, the mono oxide nanoparticles and $(Fe,Co,Ni,Cu)_3O_4$ MEO powder exhibited a reduced level of agglomeration and more finely dispersed particles on the surface of GO. Additionally, energy dispersive X-ray (EDX) mapping analysis revealed a uniform distribution of the constituent elements within the final products (Fig. S2). To conduct a more in-depth examination of the morphology of the composite structure, we utilized atomic force microscopy (AFM). Fig. S3 illustrates that several island structures, each approximately several hundred nanometers in width, have formed irregularly on the surface, creating distinct boundaries between each island. The measured film thickness is 25.8 nm. Additionally, cross-sectional observations reveal a strong bonding between the $(Fe,Co,Ni,Cu)_3O_4$ MEO and GO within the composite structure. The surface fluctuation of the island structure ranges from 13.2 nm to −12.7 nm, as depicted in Fig. S3, which demonstrates the smooth surface and the high-quality nature of the composite structure.

The FTIR spectra of the samples shown in Fig. S4 clearly illustrate the differences between pure GO and the metal oxide–GO composites. In the spectrum of GO, strong and distinct peaks corresponding to O–H stretching (around 3400 cm^{-1}), C═O stretching ($\approx$1720 cm^{-1}), C═C vibrations ($\approx$1620 cm^{-1}), and C–O–C/C–O stretching ($\approx$1050–1250 cm^{-1}) are observed. When metal oxides such as Fe_3O_4, CoO, NiO, CuO, and $(Fe,Co,Ni,Cu)_3O_4$ MEO are incorporated onto the GO surface, the characteristic GO peaks significantly decrease in intensity. This reduction indicates that the oxygenated functional groups of GO are partially consumed or modified during the formation of the composites. Additionally, the metal oxide–GO samples exhibit new or shifted vibrations in the lower-wavenumber region (below 700 cm^{-1}), which correspond to the M–O lattice stretching modes, confirming the presence of metal oxides. Fig. 2a and Fig. S5 present a comprehensive Raman spectral analysis of graphene oxide (GO) and its nanocomposites with various metal oxide nanoparticles, including Fe_3O_4–GO, CoO–GO, NiO–GO, CuO–GO, and the mixed metal oxide $(Fe,Co,Ni,Cu)_3O_4$ MEO–GO. An enhanced-resolution view of these spectra is provided in Fig. S6 (SI). The spectra exhibit two prominent bands: the D-band at 1345 cm^{-1}, associated with disorder-induced phonon modes arising from structural defects and sp^3 hybridized carbon, and the G-band at 1595 cm^{-1}, corresponding to the in-plane vibrational mode of sp^2-bonded carbon atoms in the graphitic lattice. The intensity ratio (I_D/I_G) serves as a key indicator of the degree of structural disorder and the extent of sp^2 domain restoration in GO. The observed $I_D/I_G < 1$ suggests that the MEO nanoparticles are effectively anchored onto the GO sheets, reducing the defect density and promoting partial graphitic restoration. In the Fe_3O_4–GO nanocomposite, distinct vibrational modes of magnetite (Fe_3O_4) are observed at 216 cm^{-1} (E_g), 283 cm^{-1} (T_{2g}), and 402 cm^{-1} (A_{1g}), consistent with its cubic spinel structure.[44,45] For the CoO–GO sample, the characteristic peaks at 378 cm^{-1} (F_{2g}), 452 cm^{-1} (E_g), and 667 cm^{-1} (A_{1g}) correspond to the phonon modes of rock-salt structured CoO.[46] The NiO–GO spectrum reveals three notable peaks at 536 cm^{-1}, 657 cm^{-1}, and 1077 cm^{-1}, attributed to the first-order and second-order modes of NiO, indicative of its cubic phase.[47,48] This detailed Raman analysis not only confirms the structural integrity of the synthesized nanocomposites but also highlights the distinct vibrational fingerprints of each metal oxide, reinforcing their successful incorporation into the GO framework.[49] Transmission electron microscopy (TEM) analysis of the $(Fe,Co,Ni,Cu)_3O_4$ MEO-GO nanocomposites (Fig. 2b and c) demonstrates the formation of interconnected $(Fe,Co,Ni,Cu)_3O_4$ MEO nanoparticles with an irregular polyhedral morphology. These nanoparticles appear to be uniformly distributed across the graphene oxide (GO) support, suggesting effective integration between the mixed metal oxide phase and the carbonaceous matrix. Quantitative particle size distribution analysis (Fig. S7), obtained through statistical measurement of over 200 nanoparticles from multiple TEM images, reveals a relatively narrow size distribution with an average particle diameter of 73 $\pm$ 5 nm. The observed particle size and morphology are consistent with the high surface area measured by Brunauer–Emmett–Teller (BET) analysis, and this nanoscale architecture is expected to provide numerous active sites for catalytic applications. The intimate contact between the $(Fe,Co,Ni,Cu)_3O_4$ MEO nanoparticles and the GO support, as evidenced by the TEM images, likely facilitates efficient charge transfer during catalytic processes. To assess the material adsorption capacity, the BET surface areas of the $(Fe,Co,Ni,Cu)_3O_4$ MEO and MEO–GO catalysts were evaluated using nitrogen adsorption–desorption isotherms. Fig. 2d illustrates the isotherm curves for both the $(Fe,Co,Ni,Cu)_3O_4$ MEO and MEO–GO catalysts. The MEO–GO catalyst exhibited a significantly larger surface area of 53.11 $m^2\ g^{-1}$ compared to the $(Fe,Co,Ni,Cu)_3O_4$ MEO nanoparticles, which had a surface area of 21.15 $m^2\ g^{-1}$. This increase is attributed to the dispersion of the $(Fe,Co,Ni,Cu)_3O_4$ MEO particles on the GO surface, which effectively prevents their aggregation. Fig. 2e illustrates the TGA curves of GO, $(Fe,Co,Ni,Cu)_3O_4$ MEO and MEO–GO, which were acquired at a heating rate of 10 °C min^{-1}. The TGA analysis of graphene oxide (GO) under an air atmosphere reveals three primary weight loss stages: the first (below 125 °C) corresponds to moisture evaporation, the second (125–300 °C) results from the decomposition of oxygen-containing functional groups (*e.g.*, epoxy, hydroxyl, and carboxyl), releasing CO, CO_2, and H_2O, and the third (above 300 °C) involves the combustion of the carbon skeleton, leading to near-complete oxidation with a minimal residue at ~600 °C. In contrast, $(Fe,Co,Ni,Cu)_3O_4$ medium-entropy oxide (MEO) nanoparticles exhibit exceptional thermal stability, showing negligible weight loss up to 950 °C. For the MEO–GO composite, a minor mass loss (2.1%) below

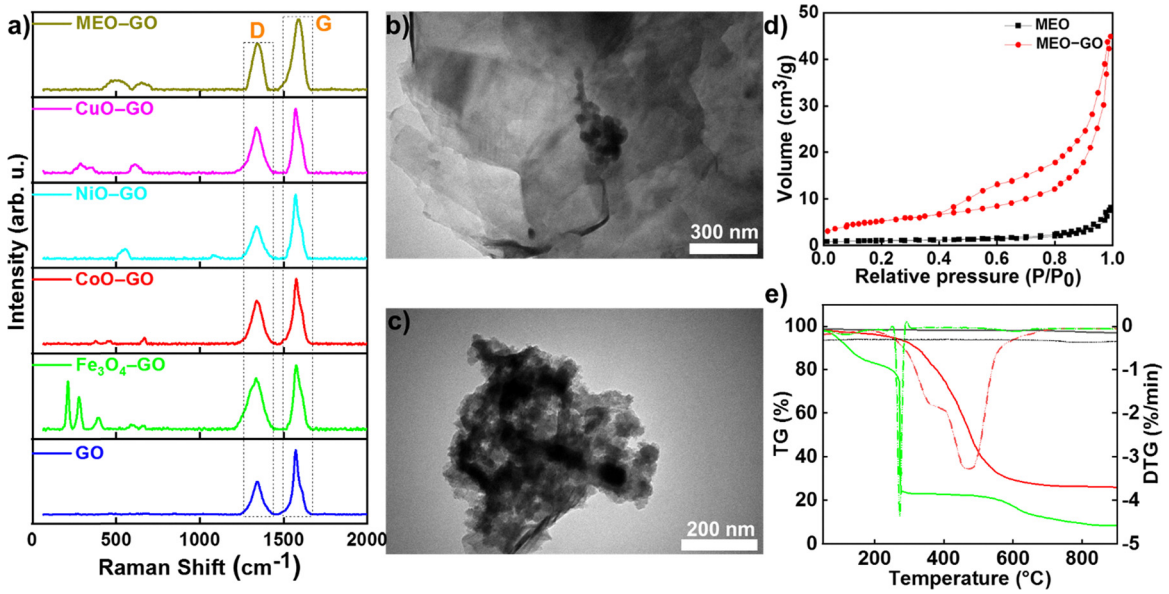

Fig. 2 (a) Raman spectra of samples, (b) and (c) TEM images of the $(Fe,Co,Ni,Cu)_3O_4$ MEO–GO sample at different magnifications showing the morphology of the nano-sized MEO on the surface of GO, (d) and (e) nitrogen adsorption–desorption isotherms and TG-DTG curves of $(Fe,Co,Ni,Cu)_3O_4$ MEO and $(Fe,Co,Ni,Cu)_3O_4$ MEO–GO samples.

180 °C is attributed to moisture desorption, while a significant weight reduction between 180 °C and 710 °C reflects GO decomposition. The TGA data indicate that the MEO–GO composite consists of approximately 25 wt% MEO nanoparticles and also suggest interactions between GO and the oxide, evidenced by shifts in decomposition temperatures compared to pure GO. This analysis highlights the enhanced thermal stability imparted by the MEO nanoparticles in the composite structure.

Fig. S8 illustrates the survey XPS spectra of MEO–GO. The primary Fe 2p doublet appears at approximately 710.5 eV and 723.7 eV (Fig. 3b), which corresponds to the spin–orbit peaks of Fe $2p_{3/2}$ and Fe $2p_{1/2}$ within an oxide chemical environment.[50] In Fig. 3b, the Co 2p spectrum reveals two spin–orbit doublets simultaneously. The doublet observed at 780.4 eV and 796.3 eV is associated with Co^{2+} and Co^{3+} oxidation states.[51] As depicted in Fig. 3c, the Ni 2p XPS spectrum presents at least two doublets, indicating that Ni is present on the surface of the MEO structure in various chemical environments.[52] The high-resolution Cu 2p XPS spectrum displays a prominent doublet at 932.6 eV and 953.6 eV, along with a satellite peak at 941.7 eV (Fig. 3d), which can be attributed to Cu^{1+} and Cu^{2+} within CuO.[53] The O 1s XPS spectrum was fitted with three bands corresponding to lattice oxygen, adsorbed oxygen species, and oxygen ions near oxygen vacancies (Fig. 3e). The significant intensity of the latter contribution suggests that the MEO–GO sample, particularly the $(Fe,Co,Ni,Cu)_3O_4$ MEO nanoparticles, possesses a high abundance of oxygen vacancies. This elevated concentration of oxygen vacancies may play a crucial role in enhancing the catalytic activity of the oxidation reaction, thereby accelerating the dehydrogenation rate of the organic substrate.[54,55] Furthermore, the C 1s XPS spectrum was fitted by considering several contributions (Fig. 3f): non-oxidized carbon at 284.3 eV with a slight downshift, carbon in the functional group of C–OH at 286.2 eV, and the carbonyl (C═O) group identified at 288.3 eV.[56]

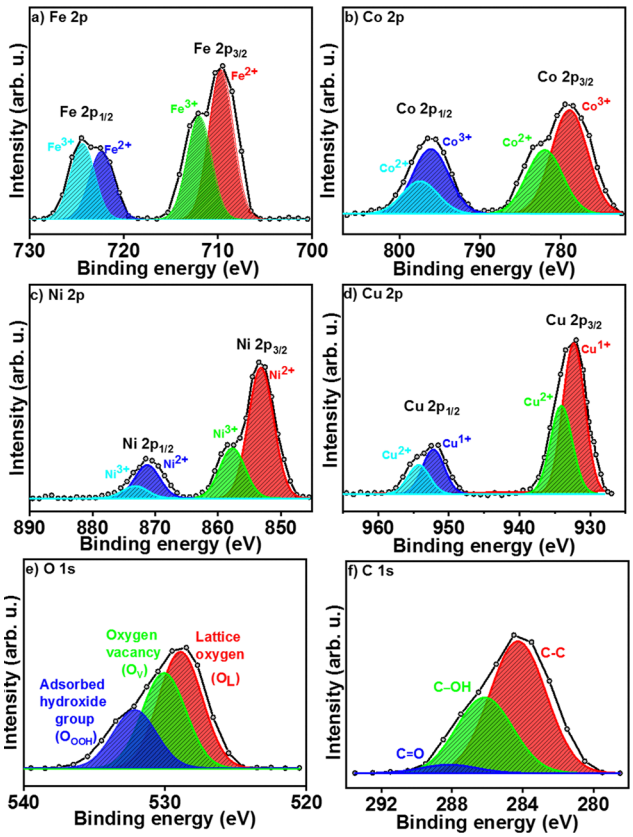

Fig. 3 High-resolution XPS spectra of $(Fe,Co,Ni,Cu)_3O_4$ MEO–GO: (a) Fe 2p, (b) Co 2p, (c) Ni 2p, (d) Cu 2p, (e) O 1s, and (f) C 1s.

3.2. Catalytic performance

Fe_3O_4–GO, CoO–GO, NiO–GO, CuO–GO, $(Fe,Co,Ni,Cu)_3O_4$ MEO–GO, and GO were employed as heterogeneous catalysts for the solvent-free oxidation of benzyl alcohol to benzaldehyde with selectivity. A range of experimental conditions were examined, including the temperature (100–140 °C), air pressure (5–20 atm), reaction duration (5–48 h), and catalyst quantity (0.2–0.6 g). The conversion and selectivity of benzyl alcohol to benzaldehyde, benzoic acid, and benzyl benzoate are presented in Table 1 and Table S1. In the absence of catalysts, a conversion rate of less than 1% was recorded under various conditions, which was markedly improved with the introduction of catalysts. The conversion of benzyl alcohol over the catalysts was found to increase with both temperature and pressure. As indicated in Table 1, all tested catalysts, including GO, Fe_3O_4–GO, CoO–GO, NiO–GO, CuO–GO, and $(Fe,Co,Ni,Cu)_3O_4$ MEO–GO, achieved a higher conversion and selectivity rates. The optimized reaction using the $(Fe,Co,Ni,Cu)_3O_4$ MEO–GO nanocomposite exhibits promising catalytic performance in the solvent-free oxidation of benzyl alcohol, achieving 17.2–28.8% conversion and 47.1–56.3% selectivity. Although the catalyst performs comparably to other noble-metal-free systems under similar conditions, the overall yield remains limited, with selectivity fluctuations of approximately ±0.05.[23,31,57–63] While noble metals (Pt and Ir) face scalability challenges due to cost and scarcity, transition metal-based systems (Ni, Cu, and Fe) and medium-entropy oxides (MEOs) offer sustainable alternatives with earth-abundant components and competitive activity.[64,65] Preliminary data suggest that these systems may reduce energy inputs and waste compared to conventional oxidants ($KMnO_4$ and H_2O_2), though further life-cycle studies are needed to fully assess their environmental and economic benefits.[66] Our MEO–GO catalyst demonstrated pressure-dependent activity in benzyl alcohol oxidation, achieving remarkable turnover numbers (TONs) of 165 and 436 under 1 atm and 20 atm air pressure, respectively, during 5 h reactions. These values correspond to turnover frequencies (TOFs) of 33 h^{-1} and 87 h^{-1}, highlighting two key findings: (1) the intrinsic high activity of our catalyst even at ambient pressure, and (2) a 2.6-fold enhancement in activity under elevated pressure (20 atm). The TON of 436 represents particularly outstanding performance, indicating that each active site facilitated nearly 450 productive reaction cycles while maintaining stability. This pressure-dependent activity boost suggests that oxygen availability is a key limiting factor in the oxidation reaction process, and that our catalyst's nanostructure remains stable under high-pressure conditions. For comparison, a catalyst composed of the holey lamellar $Co_{0.2}Ni_{0.2}Cu_{0.2}Mg_{0.2}Zn_{0.2}O$ HEO was previously noted for its superior selectivity (29%) towards benzaldehyde, operating at 1 atm O_2, 120 °C, and utilizing 10 mg of the catalyst over a 2 h period.[31] $(Fe,Co,Ni,Cu)_3O_4$ MEO–GO demonstrates enhanced selectivity relative to the holey lamellar $Co_{0.2}Ni_{0.2}Cu_{0.2}Mg_{0.2}Zn_{0.2}O$ catalyst at the same temperatures and in the presence of air rather than pure O_2.

Table 1 Aerobic and solvent-free oxidation of benzyl alcohol under different reaction conditions

				Selectivity (%)		
Entry[a]	Pressure (atm)	Catalyst	Conversion (%)	BAd	BAc	BBz
1	1	—	0.2	71.3	25.6	3.1
2	10	—	0.5	65.5	29.1	5.4
3	1	GO	5.3	53.4	31.1	15.5
4	10	GO	7.6	47.2	35.5	19.3
5	1	Fe_3O_4–GO	9.7	56.7	25.3	18.0
6	10	Fe_3O_4–GO	16.5	54.5	23.7	21.8
7	1	CoO–GO	9.6	55.1	27.8	17.1
8	10	CoO–GO	17.1	53.6	29.1	17.3
9	1	NiO–GO	9.4	56.3	24.3	19.4
10	10	NiO–GO	17.8	55.4	26.7	17.9
11	1	CuO–GO	10.1	58.1	23.4	18.5
12	10	CuO–GO	18.1	59.6	21.7	18.7
13	1	MEO–GO	17.2	71.4	15.1	13.5
14	5	MEO–GO	20.7	68.1	17.5	14.4
15	10	MEO–GO	28.8	65.7	22.1	12.2
16	20	MEO–GO	45.4	61.8	23.9	14.3

[a] Typical aerobic oxidation conditions of benzyl alcohol: 5 mL of benzyl alcohol, 0.2 g of the catalyst (actual weight ratio of $(Fe,Co,Ni,Cu)_3O_4$ MEO to GO in the synthesized nanocomposite is 1:3), rotation speed 500 rpm, under optimal pressures (air) of 1 and 10 atm and a temperature of 120 °C during 5 h. BAd: benzaldehyde, BAc: benzoic acid, and BBz: benzyl benzoate (see Fig. S6 for the GC spectrum).

Based on our earlier research, unsupported catalysts demonstrate a greater conversion rate of benzyl alcohol when compared to composite catalysts that incorporate GO; however, they exhibit a lower selectivity rate, as illustrated in Table 1. Consequently, we have also performed the oxidation reaction in a solvent-free environment utilizing composite materials as high-performance catalysts for the transformation of benzyl alcohol into benzaldehyde.

The medium-entropy oxide $(Fe,Co,Ni,Cu)_3O_4$ MEO–GO nanocomposites exhibit remarkable performance among the applied catalysts, which can be attributed to the presence of a variety of redox couples, including Fe^{2+}/Fe^{3+}, Co^{2+}/Co^{3+}, Ni^{2+}/Ni^{3+}, Cu^{1+}/Cu^{2+}, and surface oxygen species within the catalyst. These components facilitate the adsorption of oxygen species and expedite the oxidation process of benzyl alcohol.[67,68] The $(Fe,Co,Ni,Cu)_3O_4$ MEO component exhibits a high density of oxygen vacancies, which play a crucial role in the catalytic process. These vacancies, generated through the entropy-driven cation disorder characteristic of medium-entropy oxides, create electron-deficient sites that significantly enhance the adsorption and activation of benzyl alcohol molecules. The oxygen vacancies facilitate charge transfer processes and lower the activation energy for O–H bond cleavage.[69] This vacancy-mediated mechanism aligns with recent studies demonstrating how oxygen vacancies in transition metal oxides serve as active centers for alcohol oxidation reactions.[70–72] The synergistic interaction between these vacancy-rich $(Fe,Co,Ni,Cu)_3O_4$ MEO surfaces and the GO support further stabilizes the defect sites while promoting efficient electron transfer throughout the catalytic cycle. We propose that the GO present in the nanocomposites offers a significant number of active sites on its surface, which are crucial for the effective adsorption of benzyl alcohol and the subsequent desorption of oxidized products during the oxidation reaction. Additionally, within

the $(Fe,Co,Ni,Cu)_3O_4$ MEO–GO nanoparticles, the GO environment mitigates aggregation by supplying ample active surface sites that promote the selective oxidation of benzyl alcohol.[73] Moreover, the GO sheets facilitate a more profound oxidation of organic compounds and intermediates through self-decomposition, leading to the generation of reactive oxygen species.[74]

The production of free radicals is the probable mechanism for oxidizing benzyl alcohol (Fig. S9).[75–77] The oxygen vacancies on the surface of the transition metal-based $(Fe,Co,Ni,Cu)_3O_4$ MEO–GO catalyst absorb oxygen molecules and various species due to their electron deficiency.[78,79] The diffusion of benzyl alcohol to the electron-deficient catalyst surface weakens its methylene–H bond, promoting dissociation.[80] The electron-deficient metals can easily adsorb benzyl alcohol, forming the active intermediate. Meanwhile, the electron-rich GO surface stabilizes the oxygen molecule (O_2) and generates the superoxide radical ($^{\bullet}O_2^-$).[81,82] The proton (H^+) produced can yield the hydrogen peroxide radical ($HOO^{\bullet}$), which interacts with the intermediate species to form benzyl hydro-peroxide.[83,84] This hydro-peroxy radical can produce H_2O_2, which may decompose into reactive hydroxyl radicals ($HO^{\bullet}$). These then interact with benzyl alcohol to synthesize benzaldehyde *via* a free radical mechanism. A highly electron-deficient surface is essential for the selective oxidation of benzyl alcohol to benzaldehyde, which has a less basic characteristic, making it easier to desorb from the catalyst surface.[85] Additionally, the lipophilic and hydrophobic properties of the GO structure enhance the desorption of benzaldehyde from $(Fe,Co,Ni,Cu)_3O_4$ MEO–GO, making the selective aerobic oxidation of benzyl alcohol to benzaldehyde more effective due to the synergistic effects of the metal cations in the medium-entropy oxide and GO structures.

In addition, the ^1H NMR spectrum confirms that benzaldehyde is the major product (Fig. S10). The characteristic aldehydic proton appears around 9.8–10 ppm, along with the expected aromatic signals in the 7–8 ppm region. The benzaldehyde product was isolated; however, a small amount of the starting benzyl alcohol remained in the isolated fraction. A weak CH_2 signal near 4.5–5 ppm indicates the presence of this residual benzyl alcohol. EPR measurements showed the radical-based mechanism of the oxidation reaction by tracking the organic free radicals (g = 2.0023). In Fig. 4a, the EPR signal is absent at the start of the catalyst-assisted oxidation of benzyl alcohol without the solvent. However, the EPR signal appears over time, increasing in intensity as the reaction continues. This indicates that oxidation of benzyl alcohol under solvent-free conditions involves a radical-based mechanism. Additionally, we examined the impact of radical scavengers on the oxidation of benzyl alcohol. The results showed that the scavenger (NaN_3) significantly reduced the total concentration of unpaired electrons (Fig. 4a).

The stability and reusability of the $(Fe,Co,Ni,Cu)_3O_4$ MEO–GO catalyst in the aerobic oxidation of benzyl alcohol, a catalyst known for its high performance, is illustrated in Fig. 4b and c. The conversion rate of benzyl alcohol experienced a slight decline from 17.2% to 16.8%, while the selectivity for benzaldehyde decreased from 71.4% to 69.3% after undergoing 6 oxidation cycles at an air pressure of 1 atm and a temperature of 120 °C for a duration of 5 h. In addition, when subjected to an air pressure of 10 atm, the catalyst demonstrated a

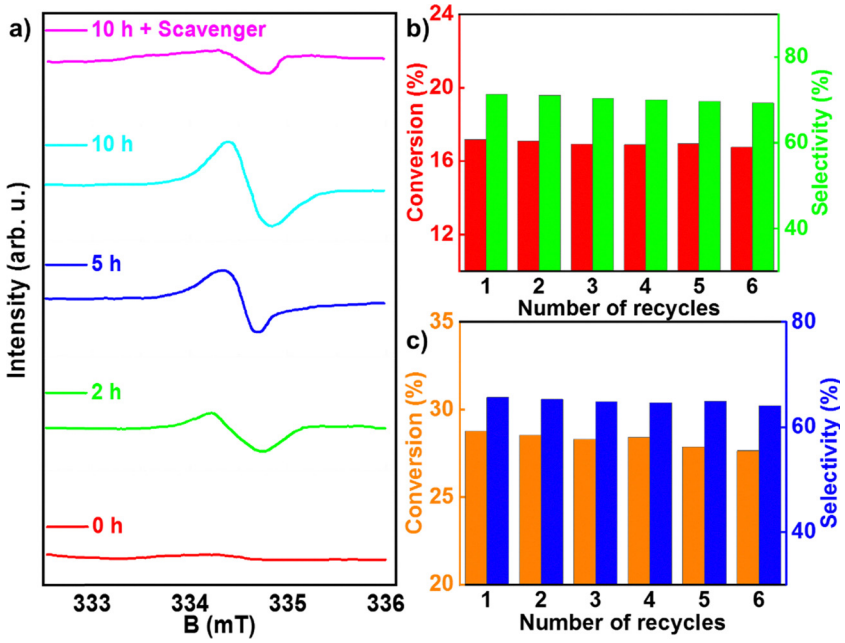

Fig. 4 (a) EPR spectra of the solvent-free oxidation of benzyl alcohol in the presence of $(Fe,Co,Ni,Cu)_3O_4$ MEO–GO as the optimum catalyst with and without a radical scavenger at ambient temperature; (b) and (c) reusability test of the $(Fe,Co,Ni,Cu)_3O_4$ MEO–GO catalyst for the solvent-free oxidation of benzyl alcohol under 1 and 10 atm.

commendable level of reusability and stability, with conversion and selectivity rates changing from 28.8% and 65.7% to 27.7% and 64.1%, respectively, after the same 6 oxidation cycles at 1 atm air pressure at 120 °C for 5 h. The $(Fe,Co,Ni,Cu)_3O_4$ MEO–GO catalyst exhibited remarkable structural and chemical stability over repeated use. This stability is strongly supported by the XRD analysis, where the characteristic diffraction peaks were largely retained after six consecutive oxidation cycles, showing only minor shifts or slight broadening. Such minimal changes indicate that the crystalline framework of the catalyst remains well-preserved during the reaction process, further confirming its robustness and suitability for repetitive catalytic applications (Fig. S11). Raman spectroscopy confirmed strong nanoparticle adhesion to GO sheets, with characteristic D (1345 cm^{-1}) and G (1595 cm^{-1}) bands and an I_D/I_G ratio below 1 (Fig. S12). Importantly, ICP analysis revealed nearly identical metal compositions before and after cycling, proving exceptional resistance to leaching or degradation (Table S2). These findings collectively demonstrate the catalyst's remarkable robustness, retaining structural integrity through repeated oxidation while preserving its active components—key attributes for high-performance catalytic applications. The decrease in rates is attributed to a slight reduction in the number of active surface sites or the surface area resulting from the aggregation of the MEO catalyst on the surface of GO. In summary, the $(Fe,Co,Ni,Cu)_3O_4$ MEO–GO catalyst shows outstanding activity and reusability for the aerobic oxidation of benzyl alcohol, positioning $(Fe,Co,Ni,Cu)_3O_4$ MEO–GO nanocomposites as highly promising candidates for selective alcohol oxidation within the chemical industry.

4. Conclusion

This study demonstrates that the entropy-stabilized $(Fe,Co,Ni,Cu)_3O_4$ MEO–GO nanocomposite acts as a practical and reusable heterogeneous catalyst for solvent-free benzyl alcohol oxidation under mild conditions, achieving 28.8% conversion and 65.7% benzaldehyde selectivity at 10 atm, enabled by the synergistic contributions of oxygen vacancies, exposed active sites, and graphene oxide stabilization. The catalyst's exceptional durability (>90% activity retention after 6 cycles) and pressure-tunable selectivity highlight its advantages over noble-metal systems, while characterization reveals three key performance factors: an entropy-stabilized defect-rich spinel structure, enhanced electron transfer from the GO support, and tailored redox properties from multimetallic synergy. These findings establish a foundation for expanding this catalytic platform to diverse alcohol oxidations, particularly for pharmaceutical intermediates and biomass transformations, with future work needed to elucidate cooperative mechanisms through kinetic/DFT studies and develop scalable synthesis protocols for industrial adoption, ultimately showcasing how entropy-driven design combined with smart support interactions can advance sustainable heterogeneous catalysis.

Conflicts of interest

There are no conflicts to declare.

Data availability

The data in this article will be available from the authors upon request.

Supplementary information (SI) is available. See DOI: https://doi.org/10.1039/d5ma01075f.

Acknowledgements

This work is based on research funded by the Iran National Science Foundation (INSF) under project No. 4037018 and by the Kazan Federal University Strategic Technological Leadership Program (PRIORITY-2030). Also, the authors are grateful to the Basic Research Program of the HSE University.

References

1 M. Stekrova, P. Mäki-Arvela, E. Leino, K. M. Valkaj, K. Eränen, A. Aho, A. Smeds, N. Kumar, K. P. Volcho, N. F. Salakhutdinov and D. Y. Murzin, *Catal. Today*, 2017, **279**, 56–62.
2 X. F. Zhang, Z. Wang, Y. Zhong, J. Qiu, X. Zhang, Y. Gao, X. Gu and J. Yao, *J. Phys. Chem. Solids*, 2019, **126**, 27–32.
3 M. Subaramanian, C. Gouda, T. K. Roy, S. Ganesan, S. Banerjee, K. Vanka and E. Balaraman, *ACS Catal.*, 2024, **14**, 8294–8309.
4 X. Xiao, C. Zheng, M. Lu, L. Zhang, F. Liu, X. Zuo and J. Nan, *Appl. Catal., B*, 2018, **228**, 142–151.
5 B. Kalita, S. Iraqui, X. Borgohain and M. H. Rashid, *RSC Adv.*, 2023, **13**, 30855–30868.
6 M. Sutradhar, M. G. Martins, D. H. B. G. O. R. Simões, R. M. N. Serôdio, H. M. Lapa, E. C. B. A. Alegria, M. F. C. Guedes da Silva and A. J. L. Pombeiro, *Appl. Catal., A*, 2022, **638**, 118623.
7 H. Wang, C. Wang, H. Yan, H. Yi and J. Lu, *J. Catal.*, 2015, **324**, 59–68.
8 Z. Wang, J. Feng, X. Li, R. Oh, D. Shi, O. Akdim, M. Xia, L. Zhao, X. Huang and G. Zhang, *J. Colloid Interface Sci.*, 2021, **588**, 787–794.
9 J. Luo, Y. Zhou, S. Yang, W. Zhu, S. Li and C. Liang, *ACS Appl. Mater. Interfaces*, 2023, **15**, 22025–22035.
10 J. C. Védrine, *ChemSusChem*, 2019, **12**, 577–588.
11 M. Gao, L. Wang, Y. Yang, Y. Sun, X. Zhao and Y. Wan, *ACS Catal.*, 2023, **13**, 4060–4090.
12 U. J. Etim, P. Bai, O. M. Gazit and Z. Zhong, *Catal. Rev.*, 2023, **65**, 239–425.
13 P. Chandra, T. Ghosh, N. Choudhary, A. Mohammad and S. M. Mobin, *Coord. Chem. Rev.*, 2020, **411**, 213241.
14 D. W. Lee and B. R. Yoo, *J. Ind. Eng. Chem.*, 2014, **20**, 3947–3959.
15 J. Shi, T. Qi, B.-C. Sun, G.-W. Chu and J.-F. Chen, *Chem. Eng. J.*, 2022, **440**, 135802.

16 X. Hu, M. Zhang, A. Ren, Y. Huang, X. Yan, R. Feng and G. Zhao, *Catal. Today*, 2022, **405–406**, 75–81.
17 Z. Ansari, S. Kadam, V. Salve, K. Patil, G. Wadhawa and P. More, *J. Mol. Struct.*, 2026, **1349**, 143761.
18 Z. Ansari, S. Kadam, S. Kasabe, J. Tripathi, P. Agale, S. Patange and P. More, *Ionics*, 2025, **31**, 8151–8172.
19 S. Arade, S. Balgude, J. Kounsalye, D. Hingane and P. More, *J. Mater. Sci.: Mater. Electron.*, 2024, **35**, 1636.
20 H. Li, H. Zhu, S. Zhang, N. Zhang, M. Du and Y. Chai, *Small Struct.*, 2020, **1**, 2000033.
21 C. Deng, T. Wang, P. Wu, W. Zhu and S. Dai, *Nano Energy*, 2024, **120**, 109153.
22 A. Ostovari Moghaddam, S. Mehrabi-Kalajahi, X. Qi, R. Salari, R. Fereidonnejad, A. Abdollahzadeh, D. A. Uchaev, E. A. Kazakova, M. A. Varfolomeev, A. Cabot, A. S. Vasenko and E. A. Trofimov, *J. Phys. Chem. Lett.*, 2024, **15**, 7577–7583.
23 S. Mehrabi-Kalajahi, A. Ostovari Moghaddam, F. Hadavimoghaddam, R. Salari, M. A. Varfolomeev, A. L. Zinnatullin, K. R. Minnebaev, D. A. Emelianov, D. A. Uchaev, R. Fereidonnejad, O. Zaitseva, G. R. Khasanova, E. A. Trofimov, A. Rozhenko, A. Cabot and F. G. Vagizov, *ACS Appl. Nano Mater.*, 2024, **7**, 5513–5524.
24 A. Ostovari Moghaddam, S. Mehrabi-Kalajahi, A. Abdollahzadeh, R. Salari, X. Qi, R. Fereidonnejad, S. A. Akaahimbe, M. Nangir, D. A. Uchaev, M. A. Varfolomeev, A. Cabot, A. S. Vasenko and E. A. Trofimov, *J. Phys. Chem. Lett.*, 2024, **15**, 5535–5542.
25 X. Fu, C. Wan, H. Huyan, S. Wang, A. Zhang, J. Zhou, H. Zhang, X. Zhao, J. Chen, X. Pan, Y. Huang and X. Duan, *EES. Catal.*, 2024, **2**, 1285–1292.
26 S. Mehrabi-Kalajahi, A. O. Moghaddam, F. Hadavimoghaddam, M. A. Varfolomeev, A. L. Zinnatullin, I. Vakhitov, K. R. Minnebaev, D. A. Emelianov, D. Uchaev, A. Cabot, I. R. Il'yasov, R. R. Davletshin, E. Trofimov, N. M. Khasanova and F. G. Vagizov, *J. Mater. Chem. A*, 2022, **10**, 14488–14500.
27 S. Mehrabi-Kalajahi, A. Ostovari Moghaddam, S. Akbarpour, S. A. H. Vasigh, B. Shaabani, M. A. Varfolomeev, M. Anandkumar, D. A. Uchaev, A. S. Vasenko and A. Cabot, *ACS Appl. Energy Mater.*, 2025, **8**, 8524–8531.
28 W. Bian, H. Li, Z. Zhao, H. Dou, X. Cheng and X. Wang, *Electrochim. Acta*, 2023, **447**, 142157.
29 J. Zhou, *Chem. Eng. J.*, 2024, **496**, 153762.
30 S. L. Fereja, Z. Zhang, Z. Fang, J. Guo, X. Zhang, K. Liu, Z. Li and W. Chen, *ACS Appl. Mater. Interfaces*, 2022, **14**, 38727–38738.
31 D. Feng, Y. Dong, L. Zhang, X. Ge, W. Zhang, S. Dai and Z. Qiao, *Angew. Chem.*, 2020, **132**, 19671–19677.
32 Y. Wei, B. Han, X. Hu, Y. Lin, X. Wang and X. Deng, *Proc. Eng.*, 2012, **27**, 632–637.
33 A. H. Falemban, I. Abdel Aziz Ibrahim, G. A. Bamagous, A. R. Alzahrani, I. Shahid, N. Shahzad, S. Hasan Hussein-Al-Ali, P. Arulselvan and I. Thangavelu, *Inorg. Chem. Commun.*, 2025, **171**, 113517.
34 J. Singh, A. Choudhury, M. Ahmad, A. Syed, S. Khan, H. A. AL-Shwaiman, L. S. Wong and D.-J. Yang, *Surf. Interfaces*, 2025, **56**, 105736.
35 K. Phiwdang, S. Suphankij, W. Mekprasart and W. Pecharapa, *Energy Proc.*, 2013, **34**, 740–745.
36 H. Lee, H. Jeong, W. Jeong, Y. J. Hwang, B. An, Y. Lee, G. Kim and D.-H. Ha, *Korean J. Chem. Eng.*, 2024, **41**, 3371–3393.
37 T. D. Desissa, M. Meja, D. Andoshe, F. Olu, F. Gochole, G. Bekele, O. A. Zelekew, T. Temesgen, B. Brehane, K. D. Kuffi and T. Hunde, *SN Appl. Sci.*, 2021, **3**, 733.
38 J. Chen, B. Yao, C. Li and G. Shi, *Carbon*, 2013, **64**, 225–229.
39 N. A. F. Al-Rawashdeh, O. Allabadi and M. T. Aljarrah, *ACS Omega*, 2020, **5**, 28046–28055.
40 J. M. P. Silva, N. F. A. Neto, A. B. Lima, M. Correa, M. R. D. Bomio and F. V. Motta, *Chem. Inorg. Mater.*, 2023, **1**, 100014.
41 C. He, X. Hu, X. Peng, Y. Zhao, Y. Li, X. Li, L. Fan and Y. Zhang, *J. Alloys Compd.*, 2023, **948**, 169780.
42 P. Majumder and R. Gangopadhyay, *RSC Adv.*, 2022, **12**, 5686–5719.
43 A. Ostovari Moghaddam, S. Mehrabi-Kalajahi, M. Moaddeli, A. Abdollahzadeh, S. A. H. Vasigh, S. A. Akaahimbe, M. Nangir, R. Fereidonnejad, B. Shaabani, M. Anandkumar, S. A. Aksenov, A. S. Vasenko and A. Cabot, *J. Phys. Chem. Lett.*, 2025, **16**, 4196–4204.
44 Y. Jiang, Z.-J. Jiang, L. Yang, S. Cheng and M. Liu, *J. Mater. Chem. A*, 2015, **3**, 11847–11856.
45 A. Ponti, C. Triolo, B. Petrovičovà, A. M. Ferretti, G. Pagot, W. Xu, V. Di Noto, N. Pinna and S. Santangelo, *Phys. Chem. Chem. Phys.*, 2023, **25**, 2212–2226.
46 K. Bindumadhavan, M. Yeh, T. Chou, P. Chang and R. Doong, *ChemistrySelect*, 2016, **1**, 5758–5767.
47 C. Li, Y. Zhu, C. Zhu, B. Li, D. Zeng, X. Wang and S. Tian, *ACS Appl. Nano Mater.*, 2025, **8**, 2711–2720.
48 M. Ranjbar-Azad and M. Behpour, *J. Mater. Sci.: Mater. Electron.*, 2021, **32**, 18043–18056.
49 J. Dąbrowa, M. Stygar, A. Mikuła, A. Knapik, K. Mroczka, W. Tejchman, M. Danielewski and M. Martin, *Mater. Lette.*, 2018, **216**, 32–36.
50 H. Zhang and G. Wang, *J. Fluoresc.*, 2025, DOI: 10.1007/s10895-025-04377-w.
51 X. Zhao, Z. Xue, W. Chen, Y. Wang and T. Mu, *ChemSusChem*, 2020, **13**, 2038–2042.
52 P. S. Bagus, C. J. Nelin, C. R. Brundle, B. V. Crist, E. S. Ilton, N. Lahiri and K. M. Rosso, *Inorg. Chem.*, 2022, **61**, 18077–18094.
53 J. A. Torres-Ochoa, D. Cabrera-German, O. Cortazar-Martinez, M. Bravo-Sanchez, G. Gomez-Sosa and A. Herrera-Gomez, *Appl. Surf. Sci.*, 2023, **622**, 156960.
54 J. Lu, J. Song, H. Niu, L. Pan, X. Zhang, L. Wang and J.-J. Zou, *Appl. Surf. Sci.*, 2016, **371**, 61–66.
55 R. Wei, M. Fang, G. Dong, C. Lan, L. Shu, H. Zhang, X. Bu and J. C. Ho, *ACS Appl. Mater. Interfaces*, 2018, **10**, 7079–7086.
56 R. Al-Gaashani, A. Najjar, Y. Zakaria, S. Mansour and M. A. Atieh, *Ceram. Int.*, 2019, **45**, 14439–14448.
57 D. I. Enache, J. K. Edwards, P. Landon, B. Solsona-Espriu, A. F. Carley, A. A. Herzing, M. Watanabe, C. J. Kiely,

D. W. Knight and G. J. Hutchings, *Science*, 2006, **311**, 362–365.
58 D. I. Enache, J. K. Edwards, P. Landon, B. Solsona-Espriu, A. F. Carley, A. A. Herzing, M. Watanabe, C. J. Kiely, D. W. Knight and G. J. Hutchings, *Science*, 2006, **311**, 362–365.
59 V. R. Choudhary, A. Dhar, P. Jana, R. Jha and B. S. Uphade, *Green Chem.*, 2005, **7**, 768.
60 N. Dimitratos, J. A. Lopez-Sanchez, D. Morgan, A. F. Carley, R. Tiruvalam, C. J. Kiely, D. Bethell and G. J. Hutchings, *Phys. Chem. Chem. Phys.*, 2009, **11**, 5142.
61 V. R. Choudhary, D. K. Dumbre, B. S. Uphade and V. S. Narkhede, *J. Mol. Catal. A: Chem.*, 2004, **215**, 129–135.
62 S. Yu, J. Li and H. Zhang, *J. Catal.*, 2022, **413**, 534–545.
63 W. Wang, R. Wang, X. Jiang, Z.-H. He, K. Wang, Y. Yang and Z.-T. Liu, *Appl. Catal., A*, 2022, **634**, 118537.
64 H. Adamu, Z. H. Yamani and M. Qamar, *Mater. Renew. Sustain. Energy*, 2022, **11**, 169–213.
65 N. Kumar, R. Aepuru, S.-Y. Lee and S.-J. Park, *Nanomaterials*, 2025, **15**, 256.
66 Y. Liu, D. Zou and Y. Gao, *J. Mater. Sci.*, 2022, **57**, 9104–9117.
67 Y. Cheng, Y. Fan, Y. Pei and M. Qiao, *Catal. Sci. Technol.*, 2015, **5**, 3903–3916.
68 D. Li, F. Ruan, Y. Jin, Q. Ke, Y. Cao, H. Wang, T. Wang, Y. Song and P. Cui, *Catal. Sci. Technol.*, 2019, **9**, 418–424.
69 W. Yang, F. Qi, W. An, H. Yu, S. Liu, P. Ma, R. Chen, S. Liu, L.-L. Lou and K. Yu, *ACS Catal.*, 2024, **14**, 5936–5948.
70 C. Triolo, S. Schweidler, L. Lin, G. Pagot, V. Di Noto, B. Breitung and S. Santangelo, *Energy Adv.*, 2023, **2**, 667–678.
71 C. Triolo, K. Moulaee, A. Ponti, G. Pagot, V. Di Noto, N. Pinna, G. Neri and S. Santangelo, *Adv. Funct. Materials.*, 2024, **34**, 2306375.
72 K. Vezzù, C. Triolo, K. Moulaee, G. Pagot, A. Ponti, N. Pinna, G. Neri, S. Santangelo and V. Di Noto, *Small*, 2025, **21**, 2408319.
73 K. Wang, J. Pang, L. Li, S. Zhou, Y. Li and T. Zhang, *Front. Chem. Sci. Eng.*, 2018, **12**, 376–382.
74 L. Li, K. Jin, C. Du and X. Liu, *RSC Adv.*, 2019, **9**, 8253–8261.
75 R. Athavale, S. Gardi, F. Choudhary, D. Patil, N. Chandan and P. More, *Appl. Catal., A*, 2024, **669**, 119505.
76 J. Li, F. Li, Q. Yang, S. Wang, H. Sun, Q. Yang, J. Tang and S. Liu, *Carbon*, 2021, **182**, 715–724.
77 P. Patil, S. Kadam, D. Patil and P. More, *J. Mol. Liq.*, 2022, **345**, 117867.
78 E. Farfan-Arribas and R. J. Madix, *J. Phys. Chem. B*, 2002, **106**, 10680–10692.
79 P. Patil, S. Kadam, D. Patil and P. More, *Catal. Commun.*, 2022, **170**, 106500.
80 J. Shi, T. Qi, B.-C. Sun, G.-W. Chu and J.-F. Chen, *Chem. Eng. J.*, 2022, **440**, 135802.
81 D. Sengupta, K. Bhowmik, G. De and B. Basu, *Beilstein J. Org. Chem.*, 2017, **13**, 1796–1806.
82 Y.-G. Wang, Y. Yoon, V.-A. Glezakou, J. Li and R. Rousseau, *J. Am. Chem. Soc.*, 2013, **135**, 10673–10683.
83 K. A. Gardner and J. M. Mayer, *Science*, 1995, **269**, 1849–1851.
84 R. H. Waldemer and P. G. Tratnyek, *Environ. Sci. Technol.*, 2006, **40**, 1055–1061.
85 D. D. Mal, S. Khilari and D. Pradhan, *Green Chem.*, 2018, **20**, 2279–2289.